coatings

MDPI

Article

Synthesis of Flower-like Crystal Nickel–Cobalt Sulfide and Its Supercapacitor Performance

Haoran Yu, Ding Shen *, Ran Zhang and Shiyu Zhao

College of Materials Science and Engineering, Liaoning Technical University, Fuxin 123000, China; 18545862961@163.com (H.Y.); 17860286036@163.com (R.Z.); 15242190567@163.com (S.Z.)
* Correspondence: shending@lntu.edu.cn

Abstract: In order to improve the pseudocapacitance performance of metal sulfide electrode materials and obtain supercapacitor energy storage devices with excellent electrochemical reversibility and long-term cycle stability, the synthesis of flower-shaped crystal nickel–cobalt sulfide and its supercapacitor performance were studied. $NiCo_2S_4$ flower-shaped crystal nickel–cobalt sulfide was prepared by the hydrothermal method with nickel foam as the raw material, and electrode materials were added to prepare supercapacitor electrodes for testing of the supercapacitor performance. The physical properties of flower-shaped crystal nickel–cobalt sulfide were tested by a scanning electron microscope and transmission electron microscope, and the voltammetric cycle and constant current charge and discharge of supercapacitor electrodes prepared from this sulfide were analyzed through experiments. The experimental results showed that the flower crystal microstructure had a positive effect on the electrochemical properties. The capacitance value was always high at different current densities, and the capacity was as high as 3867.8 A/g at pH 12. After 2000 voltage–charge–discharge cycle tests, the petal-like sulfide capacity still had a retention rate of 90.57, the flower crystal nickel–cobalt sulfide still showed an excellent supercapacitor performance and the specific capacity was still high, which demonstrates that this sulfide has excellent cyclic stability and durability in electrochemical applications.

Keywords: flower-like crystal; nickel–cobalt sulfide; synthetic preparation; supercapacitor performance; nickel foam; hydrothermal method

Citation: Yu, H.; Shen, D.; Zhang, R.; Zhao, S. Synthesis of Flower-like Crystal Nickel–Cobalt Sulfide and Its Supercapacitor Performance. *Coatings* **2024**, *14*, 564. https://doi.org/10.3390/coatings14050564

Academic Editors: Rafael Comesaña and Natalia V. Kamanina

Received: 18 March 2024
Revised: 26 April 2024
Accepted: 29 April 2024
Published: 2 May 2024

1. Introduction

The high demand for energy, increasingly scarce resources and the deteriorating ecological environment have brought serious challenges to our life. The key to overcoming these is to develop innovative energy technologies to replace traditional fossil fuels [1]. Accordingly, large amounts of resources and funds are being used to develop and promote new energy sources and to develop energy storage technologies and devices compatible with clean energy. In this context, supercapacitors have the characteristics of high efficiency, fast charge and discharge, long life, excellent power density and good environmental adaptability, among others. Their application prospects in the field of energy have attracted much attention. Supercapacitors are one of the most attractive options due to their excellent characteristics. Through continuous research and innovation, supercapacitors are expected to make important contributions to the development of clean energy and the realization of sustainable energy. Traditional capacitors store energy through static electricity, store the charge on the electrode plate of the capacitor, can instantly generate a lot of power, and complete the charge and discharge process in a very short time, but the energy density is usually low and cannot meet the needs of new energy storage devices. In order to solve the above problem, in recent decades, researchers have turned their attention to another new type of energy storage device, namely the supercapacitor [2], which combines the characteristics of the high power of traditional capacitors and high energy density of

secondary batteries and has a long cycle life. Therefore, it has become a popular research object. Supercapacitors, also known as electrochemical capacitors, are a new type of green energy storage device [3]. They combine the advantages of secondary batteries and traditional capacitors, meaning they can provide a high discharge power like traditional capacitors and have the same charge storage capacity as secondary batteries, along with the characteristics of good temperature characteristics, short charging time, long service life and environmental protection. Jiang et al. [4] prepared a three-dimensional pine cone structured Ni–Co–S_4 nanomaterial by a one-step solvothermal method. The specific capacitance of the Ni–Co–S_4 material is 2215 F/g at 0.5 A/g, and the specific capacitance retention is close to 90.2% after 10,000 cycles, showing a good cycling performance. Wang et al. [5] successfully prepared a two-dimensional nanorod array $NiCo_2S_4$ material with a nanorod as the backbone and nanowires as the branches by using the hydrothermal method. The $NiCo_2S_4$ nanorod array has a good electrochemical performance with a specific capacitance of 3093 F/g at 5 A/g and 2130 F/g at 30 A/g. At present, supercapacitors are widely used in personal consumer electronics, intelligent mobile equipment, pure electric vehicles, national defense equipment, aerospace and large-scale energy storage fields [6,7].

The key to achieving an excellent performance is to find and design a suitable electrode structure for obtaining the maximum efficiency of the proposed material. Recently, flower-like crystal nickel–cobalt sulfide as a pseudocapacitor electrode material has attracted the attention of many researchers [8]. However, the problems of slow diffusion of electrolyte ions, a low rate of performance and poor cycle stability caused by volume expansion in the electrochemical reaction of common nickel–cobalt sulfide hinder the further exploration of its energy density and power density. In view of the above analysis, in order to enhance and improve the electrochemical energy storage performance of electrode materials, relevant experts and researchers have mainly focused on the structural stability, electronic and electrolyte diffusion dynamics and other such aspects in their research, so as to improve the material, and they have promoted the application of flower crystal cobalt–nickel alloys in the field of materials science. This has laid a solid foundation for the performance improvement and wider application of supercapacitors and other equipment. Compared to elemental cobalt–nickel metal powders, floral crystal cobalt–nickel alloys exhibit excellent performance characteristics, including excellent corrosion resistance, excellent thermal stability and excellent mechanical strength. The primary advantage is the excellent corrosion resistance of the crystalline cobalt–nickel alloy material, whose crystal structure and composition enable it to resist the erosion of various corrosive media, whether acidic, alkaline or salt environments, to maintain the integrity and stability of the material. Because of this, the alloy can maintain its excellent performance under extreme working conditions and withstand an extended service life.

Secondly, the flower crystal cobalt nickel alloy material also has excellent thermal stability. It can maintain the stability and integrity of the structure at high temperatures, and it resists phase changes or lattice defects, so as to maintain the performance stability of the material. This makes it excellent in high-temperature applications and thus suitable for thermodynamically demanding fields such as the aerospace and energy industries. In addition, the flower crystal cobalt nickel alloy material also has a high mechanical strength. Its crystal structure and grain boundary characteristics give it excellent tensile, compressive and extrusion resistance. This high mechanical strength gives it an advantage in engineering structures and high-load applications, where it can withstand challenging mechanical environments and maintain its stability and reliability. Accordingly, the alloy has wide application prospects in the fields of cemented carbides, magnetic materials, fuel cells, electronic and optoelectronic devices, bioengineering materials, electromagnetic shielding and absorbing materials, etc. [9], meaning it has been widely valued by researchers for a long time. At present, the modification methods of flower-like crystal nickel–cobalt sulfide mainly include microstructural design, doping and composite structural design [10].

Pourshahmir et al. adopted nickel–cobalt layered double hydroxide/$NiCo_2S_4$/g-C_3N_4 nanohybrid material with a specific capacity of 564 F/g at a current density of

1 A/g, 1.3 times that of CoS as the electrode material, which had excellent magnification performance and high stability [11]. Rehman et al. prepared ultra-long CoS 1097 nanotube network structures by a simple one-step solvothermal method without the use of surfactants and templates. The material had hollow structure, a large specific surface area, a high specific capacity, good capacity retention and excellent Coulomb efficiency. Under the potential window of 1.5 V, the specific capacitance of 1 A/g charge and discharge was 107 F/g, the 1 A/g constant current charge and discharge lasted for 5000 cycles and the capacity retention rate was 83.3% [12]. Choi et al. successfully prepared sulfur-containing nickel–iron nanostructures using a simple hydrothermal synthesis method. At a current density of 10 mA/cm^2, the specific capacitance was 15.58 F/cm^2, compared to 3.63 F/cm^2 for the $NiCo_2S_4$ nanotube array. After 2000 cycles, the test current density was 60 mA/cm^2, and the capacity retention rate remained in the range of 79.3% [13]. Using a two-step hydrothermal method, Nakate et al. successfully prepared nanotube $NiCo_2S_4$ materials with a nanosheet coating on a foam nickel substrate. When the current density of the nanotube $NiCo_2S_4$ material was 1 mA/cm^2, the specific capacitance obtained could be as high as 1948 F/cm^2 [14].

In summary, petal-like bimetallic sulfides exhibit favorable properties; however, the current research lacks thoroughness and the underlying mechanism remains unclear. This study focuses on the hydrothermal synthesis of nickel–cobalt bimetallic sulfide materials with a flower-like lamellar structure under various alkaline pH conditions. The resulting material demonstrates exceptional performance, achieving up to 3867.8 F/g in a pH 12 environment. Even after undergoing 2000 voltage–charge–discharge cycles, the capacity of the petal-like sulfide retains an impressive rate of 90.57%. Consequently, this research contributes to realizing energy storage devices characterized by a high capacity, rapid charging capabilities and prolonged lifespan.

2. Experimental Section

2.1. Experimental Scheme

The first step was to prepare 2 cm × 5 cm cut nickel foam. Then, we cleaned it with a solution of 1 mol/L HCl. Next, we took 110 mL of deionized water and added 10 mL of HCl to form a HCl solution. The foam nickel was added to the prepared hydrochloric acid solution and ultrasound was carried out in an ultrasonic machine for no more than 3 min. We removed the nickel foam, cleaned it once with water (including HCl on the cup wall), added water, shook it by hand twice and then ultrasonicated with water for no more than 5 min. Then, ultrasound was performed with anhydrous alcohol for about 10 min. We used an air-drying box for drying (3–4 h). We marked the quality of the cleaned nickel foam. Secondly, 0.14 g nickel nitrate hexahydrate, 0.28 g cobalt nitrate hexahydrate, 0.1 g glucose and 0.1 g urea were dissolved in 60 mL deionized water in appropriate proportions to make four groups. We stirred at room temperature until completely dissolved. Subsequently, ammonia and potassium hydroxide solutions were added successively to form solutions of different pH values (pH 8, pH 10, pH 12, pH 14). We continued to stir, after completion, in four 100 mL reaction kettles, and we added the cut nickel foam to the four kettles in turn. The precursor was heated at 120 celsius for 12 h in a blast drying oven. The foam nickel was removed by hydrothermal reaction, washed with ethanol and deionized water to remove excess impurities and then dried in a blast drying oven. $NiCo_2S_4$ flower-like crystals were prepared by the hydrothermal method with sodium sulfide solution reformulated. The obtained $NiCo_2(CO_3)_{1.5}(OH)_3$ precursor was reacted with sodium sulfide (Na_2S) in a hydrothermal environment. Simply put, 0.58 g $Na_2S{\cdot}9H_2O$ was dissolved in 60 mL deionized water and placed in a 100 mL reactor, and $NiCo_2(CO_3)_{1.5}(OH)_3$ loaded on nickel foam was added. Then, the samples were heated to 180 °C for 12 h, followed by cooling to room temperature. Next, $NiCo_2S_4$ flower crystals were prepared on the surface of the nickel foam [15], washed with deionized water and ethanol and then dried at 60 °C. The process flow chart of nickel foam cleaning and flower crystal $NiCo_2S_4$ formation is shown in Figure 1.

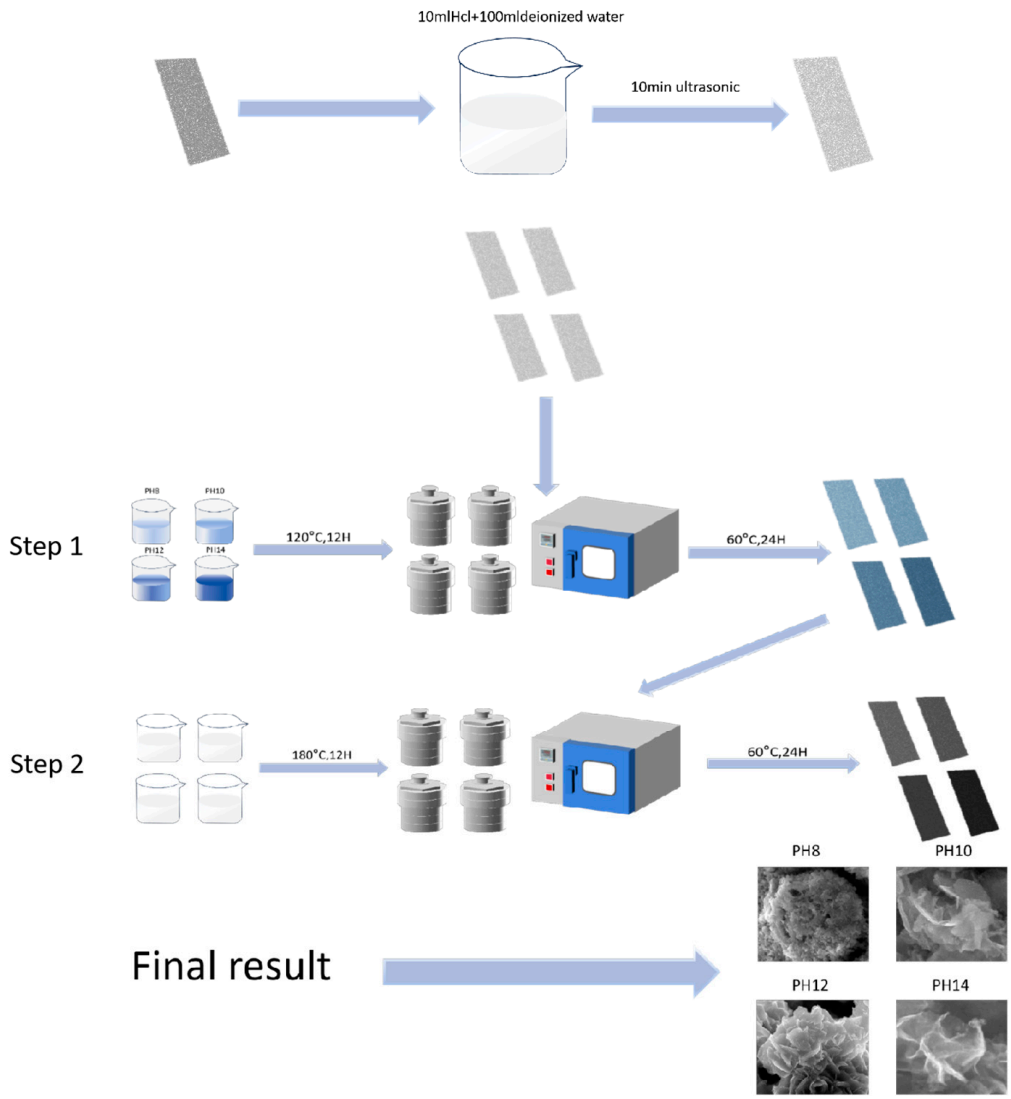

Figure 1. Illustration of the formation process of $NiCo_2S_4$.

The preparation of the electrode for the test of the electrochemical performance of $NiCo_2S_4$//AC ASC is an important part of testing materials. After much exploration and studying, the preparation process of the electrode proceeded as follows:

(1) In order to fully mix the electrode active substance and the conductive agent (acetylene black), the two are added to the mortar in a ratio and a full grinding operation is performed.

(2) The ground mixture is added to a small Petri dish, and the mass ratio is the electrode active material: acetylene black: polytetrafluoroethylene (PTFE) = 8:1:1. Next, 60 wt% PTFE emulsion is added to the Petri dish, a few drops of anhydrous ethanol are quickly added and the solution is fully stirred with a glass rod so it is evenly mixed.

(3) The Petri dish filled with the mixture is stirred with a glass rod while ultrasonicating at room temperature until the mixture is a uniform slurry with the required density.

(4) The slurry mixture is smeared on cleaned and dried foamed nickel (1 cm × 2 cm).

(5) The coated foamed nickel electrodes are placed in an oven at 60 °C for up to 24 h.

Charting the above steps, a supercapacitor electrode preparation process diagram is shown in Figure 2.

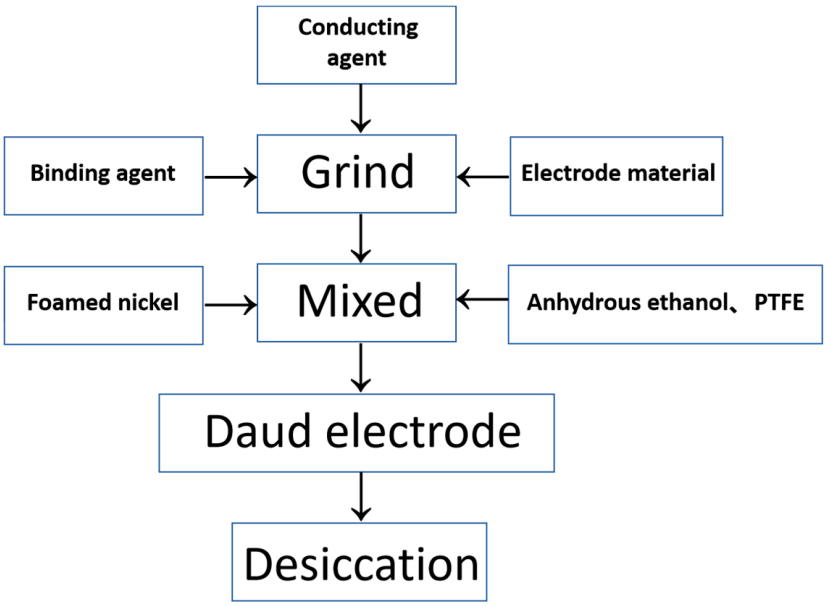

Figure 2. Supercapacitor electrode preparation process [16–18].

In order to improve the conductivity of the electrode, it is necessary to add an appropriate amount of conductive agent in the experiment. The more common conductive agents are acetylene black, carbon black and graphite powder. In this experiment, acetylene black was used as a conductive agent, and its mass was 10% of the total mass of the electrode.

2.2. Performance Analysis of 3D Flower-like Nickel–Cobalt Sulfide

2.2.1. Characterization of Physical Properties of Flower-like Crystal Nickel–Cobalt Sulfide

The phase analysis was carried out using a powder X-ray diffractometer (XRD) with a Cu tube, l = 1.54182 nm (XRD-6100 Shi-madzu, Kyoto, Japan). The morphological analysis was performed with a scanning electron microscope [19] (SEM, JEOL 7600, Akishima, Japan). The chemical properties and composition of the surface were measured by an X-ray photoelectron spectrometer (XPS, Thermo Fischer, Waltham, MA, USA). The chemical states of cobalt, nickel and sulfur were measured by XPS with Al ka radiation (1486.6 eV), and binding energies were calibrated by C 1 s (284.6 eV). The high-resolution images were taken using a transmission electron microscope [20] (TEM, Tecnai G2, FEI company, Hillsboro, OR, USA).

2.2.2. Electrochemical Performance Test of Flower-Shaped Crystal Nickel–Cobalt Sulfide

(1) Cyclic voltammetry (CV)

During the cyclic voltammetry test in this experiment, the potential window was 0~0.8 V, and the scanning speeds were 5 mV/s, 10 mV/s, 20 mV/s, 40 mV/s, 60 mV/s and 80 mV/s, respectively. The CV curve of the electrode material of the electric double layer capacitor was rectangular, and the CV curve of the pseudocapacitor had redox peaks that fluctuated up and down. The specific capacitance of the electrode material could be calculated by combining the CV curve with Formula (1):

$$C = \int IdV / mv\Delta V \tag{1}$$

In the formula, C represents the specific capacitance, I is a current under the fixed potential v, m is the quality of the active material and ΔV is a potential window.

(2) Constant current charge–discharge test (GCD)

The voltage output of electric double layer capacitors and some pseudocapacitor materials increases linearly and decreases with an increase in current, while some other pseudocapacitor materials and hybrid systems show nonlinear charging and discharging curves with one or more small, inclined voltage plateau regions. In this experiment, the potential window was 0~0.5 V, and the current densities were 1 A/g, 2 A/g, 5 A/g and 10 A/g, respectively. The specific capacitance of the electrode material could be calculated by combining the GCD curve with Formula (2):

$$C = It/m\Delta V \tag{2}$$

In the formula, C is the specific capacitance, I is the discharge current, t is the discharge time, m is the quality of the active material and ΔV is a potential window.

3. Results and Discussion

3.1. Structural Characterization

XRD was used to analyze the phase structures of samples with different pH values, and the results are shown in Figure 3. As can be seen from Figure 3, due to in situ growth on nickel foam, obvious diffraction peaks appeared at 44.50°, 51.85° and 76.38°, corresponding to the diffraction peaks of metallic nickel elements. The diffraction peaks above correspond to the crystal planes (111), (200) and (220), respectively. The diffraction peaks of binary metal sulfide NCS-pH 12 at 31.58°, 38.32°, 50.48° and 55.31° are consistent with the standard card JCPDS 73-1704 of the cubic structure $NiCo_2S_4$. The results showed that the generated material was a cubic-phase crystal $NiCo_2S_4$, and the diffraction peaks above corresponded to the crystal faces (311), (400), (511) and (440), respectively. The locations of the diffraction peaks of the binary metal sulfides NCS-pH 8, NCS-pH 10 and NCS-pH 14 were almost the same as those of NCS-pH 12, indicating that the phase of the sample was mainly $NiCo_2S_4$.

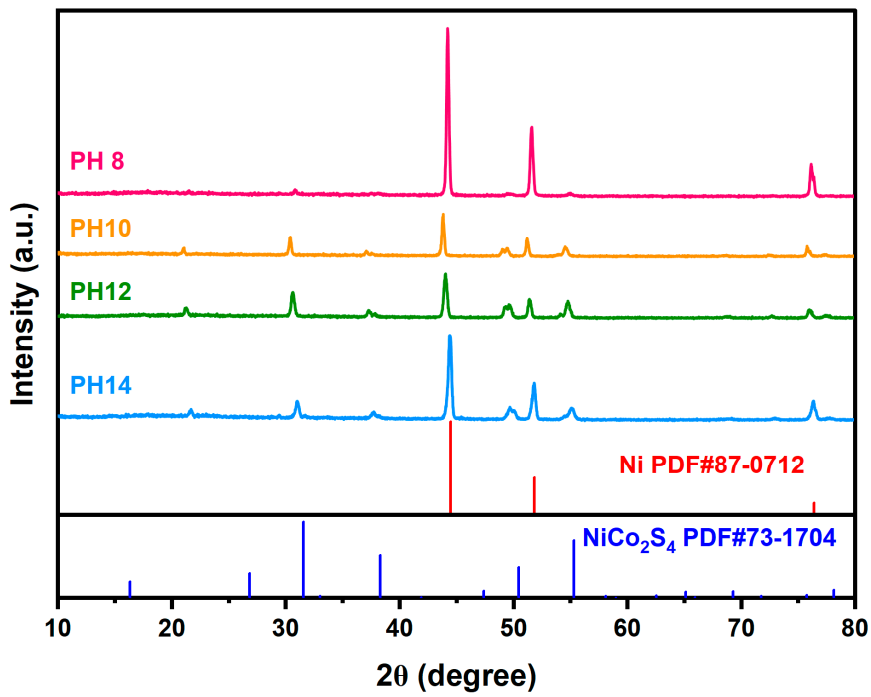

Figure 3. XRD patterns of $NiCo_2S_4$.

The elemental composition and valence distribution of NCS-pH 12 were tested by X-ray photoelectron spectroscopy (XPS) analysis, and the results are shown in Figure 4.

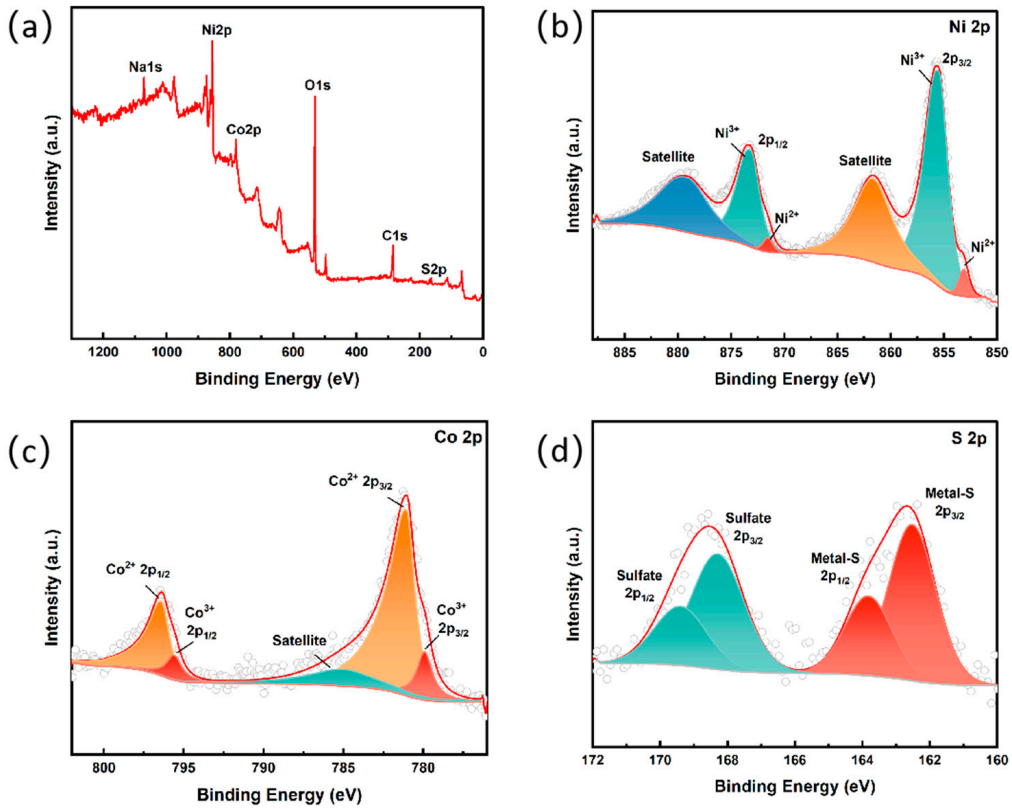

Figure 4. XPS spectra of the NCS-pH 12 sample. (**a**) Full spectrum. (**b**) High-resolution XPS spectra of Ni 2p. (**c**) High-resolution XPS spectra of Co 2p. (**d**) High-resolution XPS spectra of S 2p.

Figure 4a shows the full spectrum of NCS-pH 12, revealing that the sample contained C, O, Ni, Co and S elements. The approximate ratio of species elements was 1.22:2.41:4.05, that is, the chemical formula of the sample was $NiCo_2S_4$. As can be seen from Figure 4b, the electron binding energy positions of Ni elements were 853.13 eV and 871.54 eV, corresponding to $2p_{3/2}$ and $2p_{1/2}$ of Ni^{2+}, respectively. The electron binding energy positions 855.53 eV and 873.21 eV correspond to $2p_{3/2}$ and $2p_{1/2}$ of Ni^{3+}, respectively, known as the oxidation of the sample surface. The daughter binding energy positions 861.68 eV and 879.17 eV are the satellite peaks of Ni. The Co element electron binding energy positions 779.92 eV and 795.60 eV correspond to $2p_{3/2}$ and $2p_{1/2}$ of Co^{3+}, respectively. The electron binding energy positions 781.04 eV and 796.40 eV correspond to $2p_{3/2}$ and $2p_{1/2}$ of Co^{2+}, respectively, and the electron binding energy position 785.07 eV is the satellite peak of Co. The electronic binding energy positions of the S element are 162.53 eV and 163.83 eV, corresponding to $2p_{3/2}$ and $2p_{1/2}$ of Metal-S, respectively. The electron binding energy positions of 168.30 eV and 169.40 eV correspond to $2p_{3/2}$ and $2p_{1/2}$ of sulfate (metal sulfate), respectively. The above results further confirmed the formation of mixed-metal $NiCo_2S_4$, which was not only consistent with the XRD analysis but also consistent with the reports in the literature [21].

3.2. SEM Micro-Morphology and TEM Ultra-Micro-Morphology

The morphology of the nickel–cobalt compounds was characterized by SEM. Figure 5a–h show scanning electron microscope (SEM) photos of the nickel–cobalt compounds at different magnifications at pH 8, 10, 12 and 14.

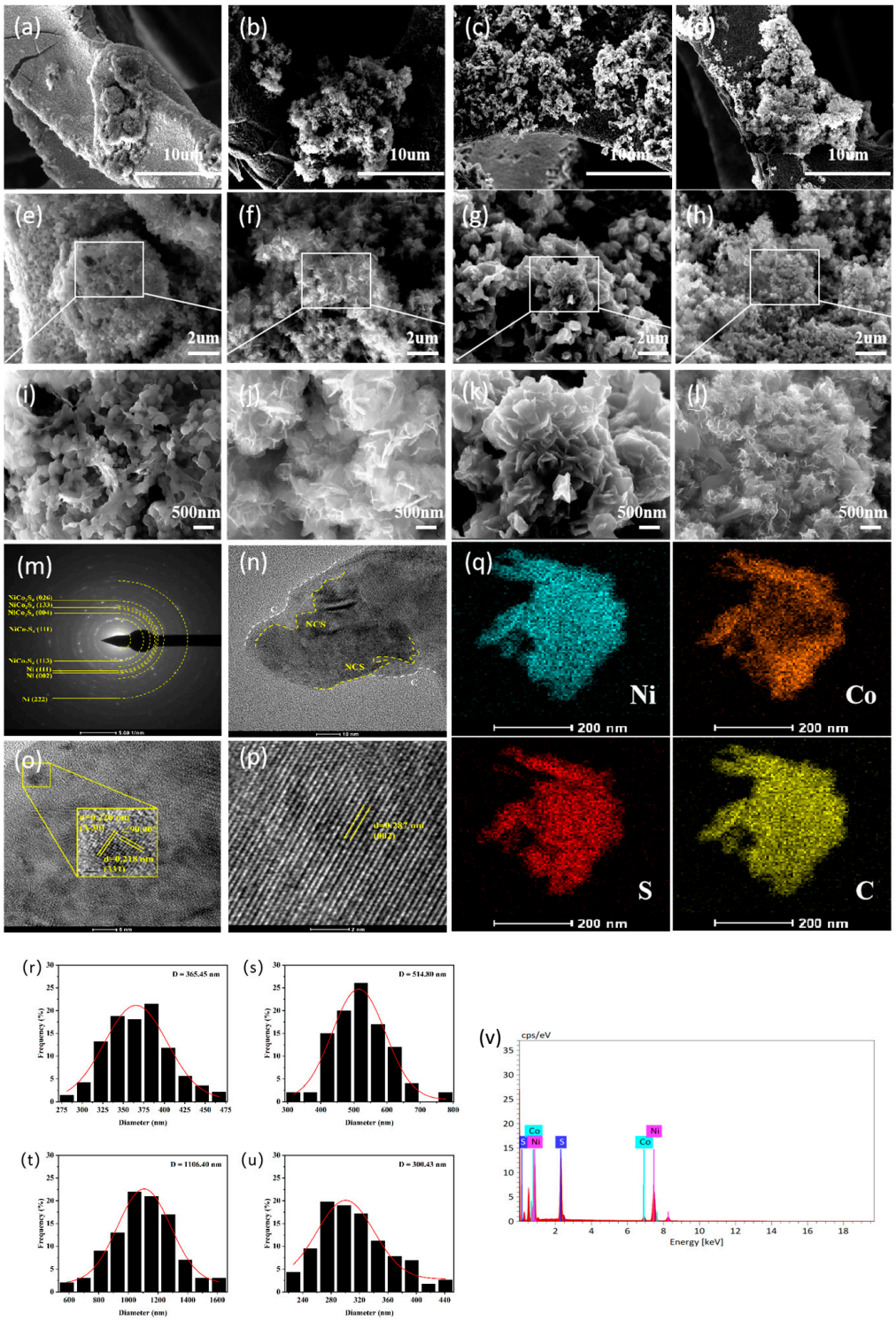

Figure 5. (**a**–**d**) SEM image at 5 k pH 8–pH 14 magnification. (**e**–**h**) SEM image at 10 k pH 8–pH 14 magnification. (**i**–**l**) SEM image at 30 k pH 8–pH 14 magnification. (**m**–**p**) Magnification TEM image. (**q**) Elemental mapping of the floral crystal nickel–cobalt sulfide. (**r**–**u**) Particle size analysis diagram. (**v**) EDS elemental analysis diagram.

Based on the microscopic morphology shown in Figure 5, flower-like crystalline NiCo compounds exhibited a tight in situ growth arrangement on the surface of nickel foam, with the neat and orderly distribution resembling a flower-like crystal structure. This unique shape provided a significantly enlarged specific surface area, which was favorable for facilitating electrochemical reactions. Figure 5a–d show SEM images of pH 8–pH 14 at 5 k, proving that the generated material was in situ grown on the surface of nickel foam. It can be seen from Figure 5e–h that there were different void sizes in the microstructure. The microstructure under pH 12 had many voids, a large specific surface area and the highest crystallinity, and the flower-like crystal structure was the most complete. The morphologies of flower-like crystalline NiCo compounds varied under different alkaline solutions. At pH 8 (Figure 5i), the NiCo compounds appeared in a spherical state without expansion; at pH 10 (Figure 5j), they exhibited a semi-open state; and at pH 12 (Figure 5k), they presented a fully blooming state with a dense distribution. The formation of this distinct morphology and structure can be attributed to the rapid anion exchange reaction during the preparation process of $NiCo_2S_4$ compounds in an alkaline environment, where new phases are formed, leading to the gradual expansion of petals and resulting in an increased specific surface area. In contrast, at pH 14 (Figure 5l), the flower-like crystal NiCo compounds showed contraction. It can be concluded that an alkaline environment with pH 12 is most suitable for obtaining flower-like crystal $NiCo_2S_4$ structures.

In order to observe the ultrastructure of the sample, the flower-like crystalline nickel–cobalt compound was tested and analyzed by transmission scanning electron microscope (TEM). The ultrastructure of the flower-like crystalline nickel–cobalt compound at different distances is shown in Figure 5. Figure 5m shows the crystal plane analysis corresponding to XRD; Figure 5n shows that some of the carbon element was coated on the outside of $NiCo_2S_4$, caused by the addition of glucose in the reaction; Figure 5o shows nickel–cobalt compounds of flower crystals with lattice stripes or with more dispersed particle structures, which are conducive to the generation of electrochemical reactions. The measured crystal face spacing was 0.22 nm or 0.218 nm, respectively, and the crystal face angle was 90°, corresponding to the (3–30) and (331) crystal faces of a certain phase, respectively. Figure 6f shows the void lattice spacing of nickel foam. Figure 5q shows the elemental mapping of the floral crystal nickel–cobalt sulfide. By measuring the SEM image and then calculating particle size analysis data through the program, we produced Figure 5r–u, which are analysis diagrams of the particle size. We can see that the particle size was different under different pH values, and its law and capacity change were the same. With an increase in pH value, the particle size first increased and then decreased, and the maximum was reached at pH 12. Figure 5v is an EDS elemental analysis diagram, which shows that the specific ratio of nickel–cobalt–sulfur was 1.32:2.6:3.92. This was slightly different from the XRD results but the proportions were similar; since the equipment was different, a certain error was expected.

3.3. Electrochemical Performance Analysis

The potential window of the cyclic voltammetry test was 0 V–0.8 V, and the potential window of the constant current charge–discharge test was 0 V–0.5 V. The cyclic voltammograms at scanning rates of 5 mV/s, 10 mV/s, 20 mV/s, 40 mV/s, 60 mV/s and 80 mV/s are shown in Figure 6.

It can be clearly seen from Figure 6a that, in terms of the integral area of the cyclic voltammetry (CV) curve, NCS-pH 12 had the largest integral area among the four ratios, so it had the longest discharge time. The cyclic voltammetry curve has an obvious redox peak, which indicates that all metals had redox reactions during charge and discharge. This was due to the change in the valence of Ni^{2+}/Ni^{3+}, Co^{2+}/Co^{3+} and Co^{3+}/Co^{4+} in the metal surface electrode material, which is a pseudocapacitance characteristic [22].

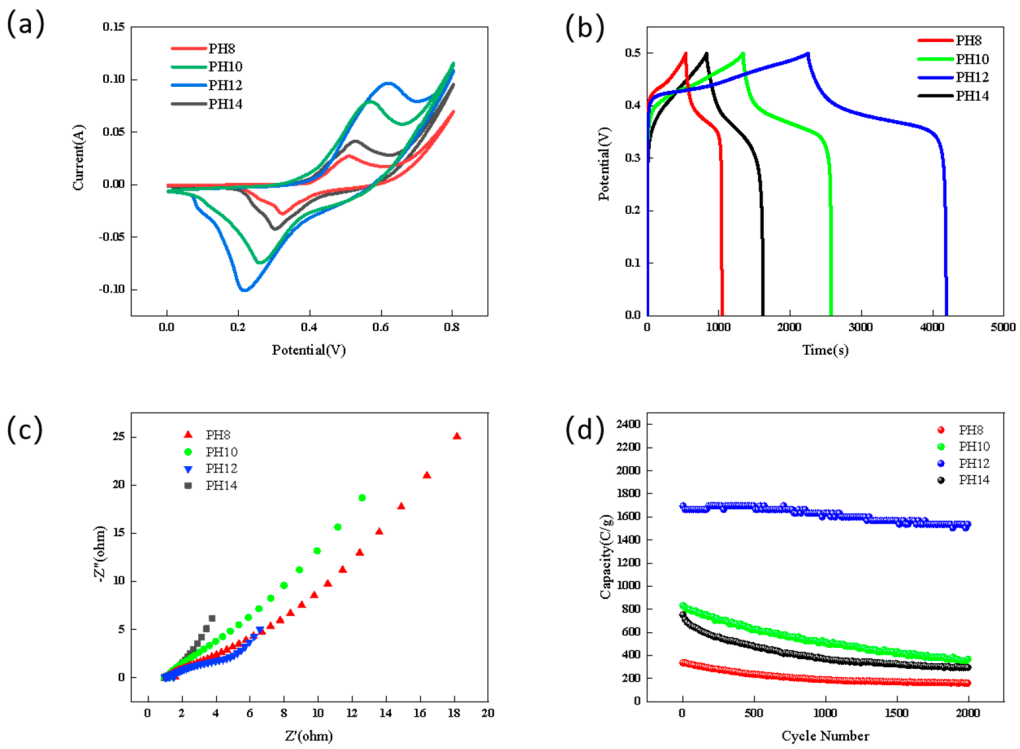

Figure 6. Electrochemical properties of metal sulfides at different pH values. (**a**) Cyclic voltammetry (CV) curves of metal sulfides at 5 mV/s. (**b**) Constant current charge-discharge curves of metal sulfides. (**c**) Electrochemical impedance spectra of metal sulfides. (**d**) Cycle performance curves of metal sulfides after 2000 cycles.

As calculated from Figure 6b, the specific capacities of NCS-pH 8, NCS-pH 10, NCS-pH 12 and NCS-pH 14 were 1584.1 F/g, 2476.2 F/g, 3867.8 F/g and 1012.1 F/g, respectively. It can be seen from the above-calculated specific capacity data that NCS-pH 12 had the largest specific capacity at 3867.8 F/g. Under different alkaline conditions, its specific capacity first increased and then decreased, and it reached the peak value at NCS-pH 12. The reason for this result is that different alkaline pH values will affect the microscopic morphology differently and, in turn, the performance. According to the above particle size analysis, the average particle size under pH 12 was the largest, so the performance was the best.

According to the information shown in Figure 6c, we conducted an in-depth analysis of the impedance spectrum of nickel–cobalt nanospheres. It can be seen from the figure that the impedance spectrum of nickel–cobalt nanospheres was clearly divided into a high-frequency region and low-frequency region, which reflected the electrical characteristics of the material at different frequencies. Nickel–cobalt nanospheres exhibited the greatest resistance at pH 8. This may have been due to the fact that in this pH environment, electron transport or ion migration within the material was restricted to a greater extent, resulting in an increase in resistance. This phenomenon may reveal the conductive properties of the material under specific acid-base conditions. However, when the pH was raised to 14, we observed the biggest change in resistance. This means that the electrical properties of nickel–cobalt nanospheres change significantly in a strongly alkaline environment. This change may be caused by changes in the surface charge state of the material, ion adsorption or chemical reactions. In addition, the strong alkaline environment may have affected the electronic structure and conductive channels inside the material, which triggered a significant change in resistance. Cycle performance is an important parameter for evaluating the electrochemical performance of supercapacitors.

Figure 6d shows the cycle performance curve at a current density of 10 A/g. During the 2000 cycles, samples of NCS-pH 8, NCS-pH 10, NCS-pH 12 and NCS-pH 14 maintained 42.3%, 38.29%, 90.57% and 47.62% of the first specification capacity, respectively. The results showed that NCS-pH 12 with $NiCo_2S_4$ as the main sample had the best structural stability and cycle performance. In particular, the specific capacity of the NCS-pH 12 sample still had a high retention rate after 2000 cycles, and the specific capacitance of sample NCS-pH 12 gradually decreased after 500 cycles. This phenomenon may have been due to the large surface area of the sample, meaning the electrolyte took some time to effectively penetrate the active electrode material [23].

In order to further evaluate the capacitive performance of NCS-pH 12, the cyclic voltammetry and constant current charge–discharge of NCS-pH 12 were tested, and the results are shown in Figure 7. Figure 7a shows the cyclic voltammetry curves of NCS-pH 12 under different rates of scans in the range of 5~80 mV/s. At a low scanning rate of 5 mV/s, a pair of strong redox peaks can be observed near 0.37 V and 0.22 V, indicating that the specific capacitance was mainly attributable to the rapid reversible electrochemical redox reaction process of the Co^{2+}/Co^{3+} and Ni^{2+}/Ni^{3+} redox pairs, with the reaction formula as follows [24,25].

$$NiCo_2S_4 + OH^- + H_2O \longleftrightarrow NiS_{(4-4x)}OH + 2CoS_{2x}OH + e^- \quad (3)$$

$$CoS_{2x}OH + OH^- \longleftrightarrow CoS_{2x}O + H_2O + e^- \quad (4)$$

$$CoS_{2x} + OH^- \longleftrightarrow CoS_{2x}OH + e^- \quad (5)$$

$$NiS_{(4-4x)} + OH^- \longleftrightarrow NiS_{(4-4x)}OH + e^- \quad (6)$$

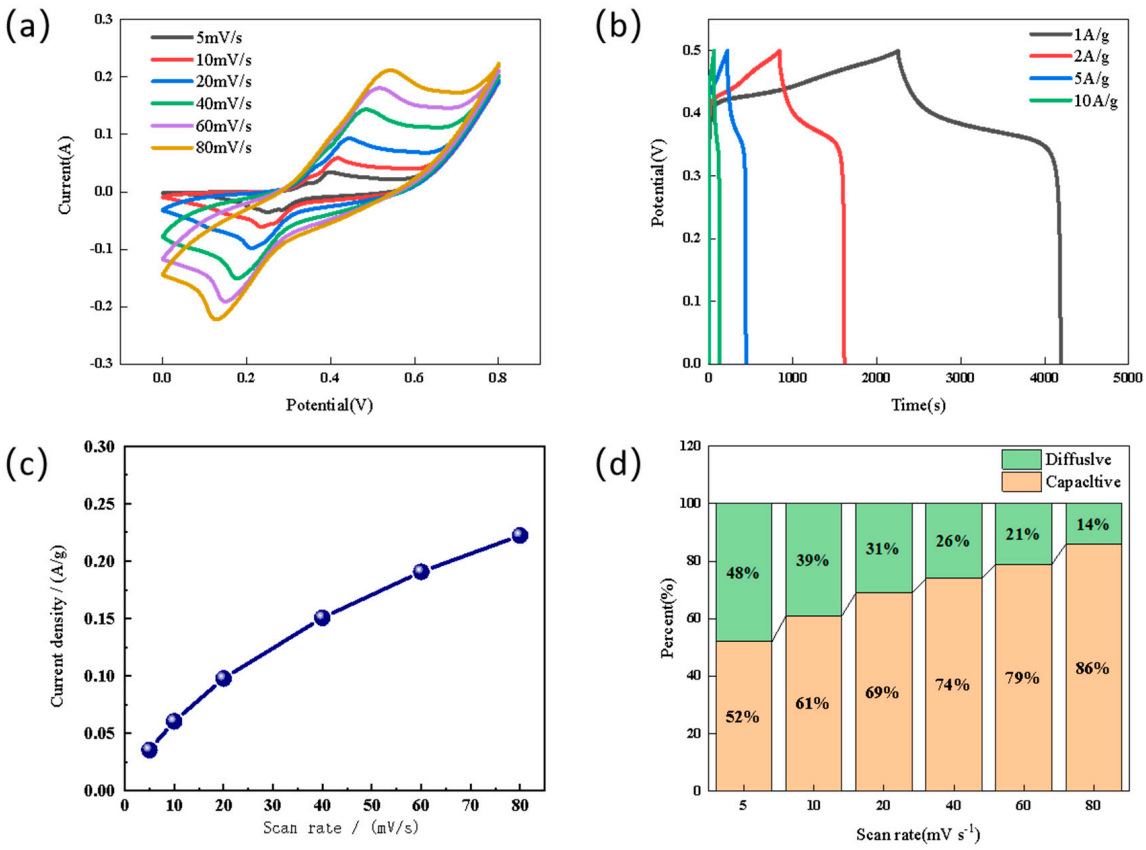

Figure 7. The electrochemical performance of the NCS-pH 12 sample. (**a**) Cyclic voltammetry (CV) curves. (**b**) Constant current charge–discharge curves. (**c**) Relationship between scanning rates and the current density. (**d**) Contribution rates of diffusion and surface capacitance.

With an increase in scanning rate, the oxidation peak and reduction peak moved to a high potential and low potential, respectively, because the ions in the electrolyte were not fully embedded in the electrode material [26].

Figure 7b shows the constant current charge and discharge curve of NCS-pH 12 under different current densities. When the current densities were 1, 2, 5 and 10 A/g, the specific capacitance values were 3867, 3099, 2183 and 1266 F/g, respectively, due to the low current densities. So, ions could fully diffuse into all the pores inside the electrode material. With the continuous increase in current density, the effective contact between ions and electrodes gradually decreased, resulting in a decrease in specific capacitance [27]. As shown in Figure 7b, the constant current charge and discharge curve of NCS-pH 12 did not undergo obvious shape changes with the continuous increase in current density, and maintained symmetry, which indicates that the NCS-pH 12 electrode material had high Coulomb efficiency and good stability [28]. It should be noted that the specific capacity of the NCS-pH 12 sample exceeded the theoretical capacity of $NiCo_2S_4$, which may have been caused by the synergistic effect of the pseudocapacitance formed by the flower crystal structure and the electric double layer capacitance [29,30].

The relationship between different scanning rates (n) and current densities (i) at the reduction peak was obtained from Figure 7a, as shown in Figure 7c. The charge and discharge mechanism could be qualitatively evaluated by the following formula:

$$i = aV^b \tag{7}$$

where a and b are tunable constants. Generally, when b is 0.5, diffusion control dominates in the charge and discharge process, and when b is 1, surface control dominates. The measured result was 0.57 ± 0.05, ranging from 0.5 to 1 [31]. The result showed that the redox process of NCS-pH 12 samples composed of $NiCo_2S_4$ was controlled by diffusion and surface capacitance.

Figure 7d further shows the diffusion rates and the contributions of surface capacitance of $NiCo_2S_4$ in the redox process at different scanning speeds. With an increase in scanning rate, the ion diffusion contribution of the redox reaction of the $NiCo_2S_4$ electrode increases, indicating that the $NiCo_2S_4$ electrode has certain electrochemical properties [32].

3.4. Electrochemical Performance of $NiCo_2S_4$//AC ASC

In order to determine its suitability for practical application, an ASC device with $NiCo_2S_4$ as the positive electrode and AC as the negative electrode was constructed. Considering the individual electrochemical stabilities of the two electrodes, the $NiCo_2S_4$//AC device was constructed by measuring the CV at 10 mV/s in a three-electrode system, and the results are shown in Figure 8a. The potential window of the $NiCo_2S_4$ electrode was 0–0.5 V, and the AC window was −1–0 V, indicating that the total working potential window of the $NiCo_2S_4$//AC device could reach 1.5 V, which confirmed that the appropriate working potential window of the $NiCo_2S_4$//AC device was 0–1.5 V. CV curves of $NiCo_2S_4$//AC were collected at different scanning rates, and the results are shown in Figure 8b. It is shown that the CV curve shape between 5 and 60 mV/s has no obvious distortion, which indicates that ASC devices have a stable current response even at 60 mV/s due to the fast electron and ion transport rates [33]. As shown in Figure 8c, the GCD profiles at different current densities exhibited a symmetrical triangular shape and a slight voltage plateau, supporting the conclusion of the previous CV analysis that the device had good electrochemical reversibility. At 1 A/g, the Cs was calculated as 365.3 F/g (Figure 8e), which remained at about 68.56% at high a Coulomb efficiency (93% at 10 A/g). At the same time, the long-term cycle stability of the ASC unit at 10 A/g was also tested for 2000 cycles (Figure 8d). The specific capacitance (310.33 F/g for 1 cycle) of the ASC device maintained a retention rate of 88.75% and a Coulomb efficiency of 94.16% after 2000 cycles, indicating good cycle performance at a high current density. When the power density was 750 W/kg, the maximum energy density was 114.17 Wh/kg, and when the power density was 7500 W/kg, the energy density remained at 87.29 Wh/kg, which showed a high energy

storage application potential. As shown in Figure 8f, the Ragone chart revealed that the performance of $NiCo_2S_4$//AC was comparable with and even higher than those for reported supercapacitors. The symmetrical supercapacitor assembled by the $NiCo_2S_4$ nanotube array showed a high energy density of 87.29 Wh/kg. These values are higher than those reported in the existing literature about $Ni_xCo_yS_z$ metal sulfides and their composites for supercapacitors, as shown in Table 1. Thus, the reported strategies may attract widespread interest in the research field of electrode materials for high-energy-density supercapacitors.

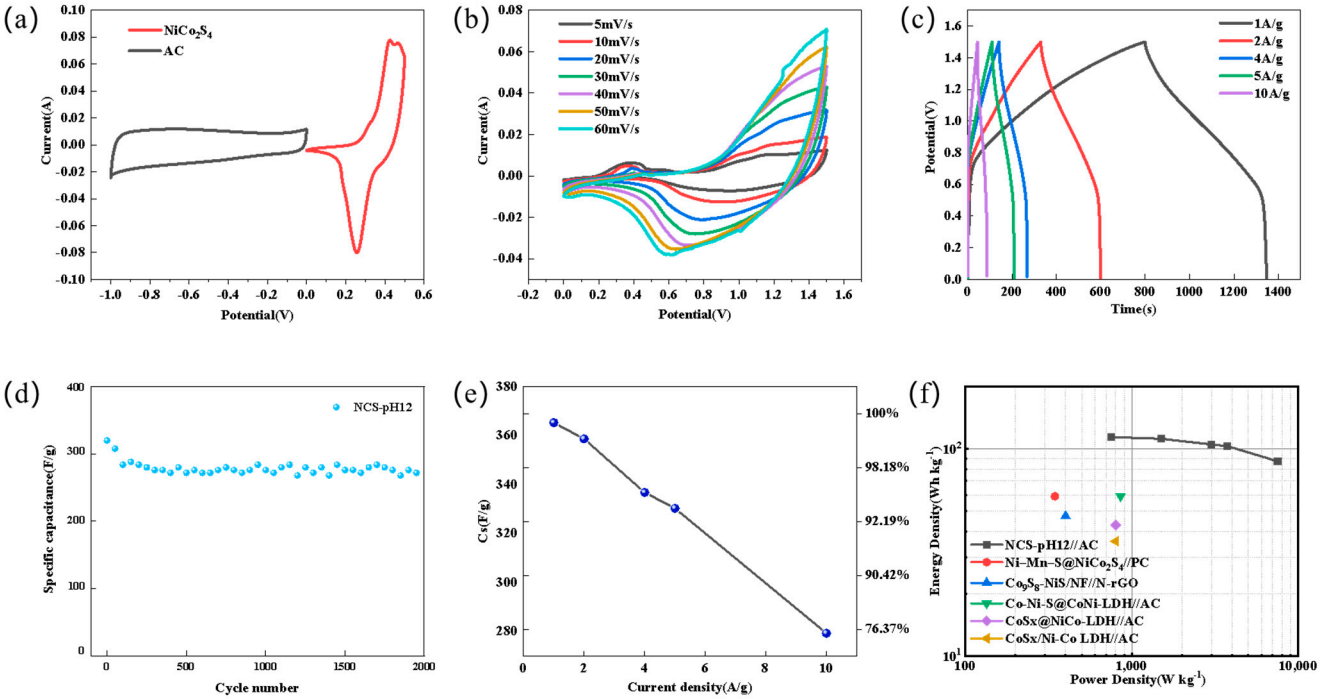

Figure 8. (**a**) Positive and negative cyclic voltammetry (CV) curves of AC and $NiCo_2S_4$ electrodes at 10 mV/s, (**b**) CV curves at different scan rates, (**c**) GCD curves at different current densities; (**d**) long-term cyclic stability at 10 A/g for 2000 cycles; (**e**) specific capacitance levels at different current densities; (**f**) Ragone plots of the ACS device compared to those in the literature.

Table 1. Capacitance properties of nickel–cobalt sulfides and their composites with different morphologies.

Material	Morphology	Specific Capacitance	Cycling Performance	Energy Density	Ref.
$CoNi_2S_4$	mushroom	5.71 F/g at 20 mA/cm^2	80.9% after 3000 cycles	---	[27]
$NiCo_2S_4$	nanotube arrays	15.58 F/cm at 10 mA/cm^2	79.3% after 2000 cycles	---	[34]
r-$NiCo_2S_4$	hollow spheres	763.5 C/g at 1 A/g	91.40% after 5000 cycles	50.76 Wh/kg at 800 W/kg	[35]
$NiCo_2S_4$	sheet-like	971 F/g at 2 A/g	88.7% after 3500 cycles	---	[36]
NF/G/Ni-Co-S	flower-like nanosheets	2526 F/g at 2 A/g	77.0% after 2000 cycles	---	[37]
$NiCo_2S_4$	nanoparticles	630.6 F/g at 1 A/g	110% after 10,000 cycles	19.35 Wh/kg at 235.0 W/kg	[38]
$NiCo_2S_4$	sea-urchin-like	1334 F/g at 0.5 A/g	91.9% after 2000 cycles	37.32 Wh/kg at 317.8 W/kg	[39]
$NiCo_2S_4$	nanoparticles	742.9 C/g at 1 A/g	83.78% after 5000 cycles	53.00 Wh/kg at 850 W/kg	[40]
$Ni_{1.64}Co_{2.40}S_4$/rGO		1089 F/g at 1 A/g	92.6% after 10,000 cycles	30.4 Wh/kg at 10 KW/kg	[41]

In summary, a series of nickel–cobalt metal sulfides were synthesized by a two-step hydrothermal method. Nickel–cobalt metal sulfides are of great significance in terms of morphology, composition, structure and electrochemical properties. The NCS-pH 8, NCS-pH 10, NCS-pH 12 and NCS-pH 14 samples were all composed of $NiCo_2S_4$. The NCS-pH 12 sample composed of $NiCo_2S_4$ had excellent electrochemical properties. These were due to the rapid ion diffusion properties of $NiCo_2S_4$, which has a flower-like crystal structure, as determined by AC impedance spectroscopy. The above results show that the assembled symmetrical devices have broad application prospects in high-energy-density supercapacitors.

4. Conclusions

A flower-like crystalline nickel–cobalt sulfide was synthesized and its supercapacitor performance was tested on an electrochemical workstation. The results showed that the flower-like crystalline nickel–cobalt sulfide products prepared in this study had a high specific capacity and good cycle performance. Using nickel foam as the conductive substrate, firstly, a nickel–cobalt precursor was synthesized on the substrate by the hydrothermal method, and a flower-like crystalline nickel–cobalt compound $NiCo_2S_4$ was prepared by using this precursor. A $NiCo_2S_4$ electrode was prepared by an ion exchange reaction between the nickel–cobalt precursor and Na_2S. The electrochemical performance test showed that $NiCo_2S_4$ was prepared in this study. The morphologies of the material were determined in different alkaline environments. In a suitable alkaline environment, a good microstructure was formed, which improved the electrical conductivity and power density of the product.

In this study, a flower-like crystalline nickel–cobalt compound $NiCo_2S_4$ was successfully prepared by the hydrothermal method, which expands the idea of improving the energy density of capacitive electrode materials through modification.

Author Contributions: Data curation, writing—original draft, H.Y.; methodology, D.S.; writing—review and editing, R.Z.; software, resources, S.Z. All authors have read and agreed to the published version of the manuscript.

Funding: This research received no external funding.

Institutional Review Board Statement: Not applicable.

Informed Consent Statement: Not applicable.

Data Availability Statement: Data are contained within the article.

Conflicts of Interest: The authors declare no conflict of interest.

References

1. Suo, N.; Dou, Z.; Cui, L. Interface and composition engineering of vanadium doped cobalt nickel sulfide/phosphide heterostructure for efficient water splitting. *Electrochim. Acta* **2021**, *368*, 137602. [CrossRef]
2. Hou, P.; Yang, Y.Y.; Li, H.Q. Study of Energy Storage System Model Selection and Simulation Based on Supercapacitor. *Comput. Simul.* **2022**, *39*, 148–152+159.
3. Yin, Y.; Fang, Z.; Chen, J.; Peng, Y.; Zhu, L.; Wang, C. Hybrid li-ion capacitor operated within an all-climate temperature range from −60 to +55 °C. *ACS Appl. Mater. Interfaces* **2021**, *13*, 45630–45638. [CrossRef]
4. Jiang, J.; Sun, Y.; Chen, Y.; Hu, X.; Zhu, L.; Chen, H.; Han, S. One-step synthesis of nickel cobalt sulfide nanostructure for high-performance supercapacitor. *Mater. Sci.* **2019**, *54*, 11936–11950. [CrossRef]
5. Wang, S.; Zhang, P.; Liu, C. Synthesis of hierarchical bimetallic sulfide $NiCo_2S_4$ for high-performance supercapacitors. *Colloids Surf. A* **2021**, *616*, 126334. [CrossRef]
6. Aadil, M.; Nazik, G.; Zulfiqar, S.; Shakir, I.; Aboud MF, A.; Agboola, P.O.; Warsi, M.F. Fabrication of nickel foam supported cu-doped Co_3O_4 nanostructures for electrochemical energy storage applications. *Ceram. Int.* **2021**, *47*, 9225–9233. [CrossRef]
7. Pinthurat, W.; Hredzak, B. Fully decentralized control strategy for heterogeneous energy storage systems distributed in islanded dc datacentre microgrid. *Energy* **2021**, *231*, 120914. [CrossRef]
8. Yan, F.; Yan, L.; Wei, X.; Han, Y.; Huang, H.; Xu, S. Structure-design and synthesis of nickel-cobalt oxide/sulfide/phosphide composite nanowire arrays for efficient overall water splitting. *Int. J. Hydrogen Energy* **2022**, *47*, 10616–10627. [CrossRef]
9. Zhang, X.; Li, B.; Lan, M.; Yang, S.; Xie, Q.; Xiao, J. Cation modulation of cobalt sulfide supported by mesopore-rich hydrangea-like carbon nanoflower for oxygen electrocatalysis. *ACS Appl. Mater. Interfaces* **2021**, *13*, 18683–18692. [CrossRef]
10. Hekmat, F.; Ezzati, M.; Shahrokhian, S.; Unalan, H.E. Microwave-assisted decoration of cotton fabrics with nickel-cobalt sulfide as a wearable glucose sensing platform. *J. Electroanal. Chem.* **2021**, *890*, 115244. [CrossRef]
11. Pourshahmir, M.; Ghasemi, S.; Hosseini, S.R. Nickel-cobalt layered double hydroxide/$NiCo_2S_4$/g-C_3N_4 nanohybrid for high performance asymmetric supercapacitor. *Int. J. Hydrogen Energy* **2023**, *48*, 8127–8143. [CrossRef]
12. Rehman, M.U.; Manan, A.; Khan, M.A.; Uzair, M.; Qazi, I.; Iqbal, Y. Improved energy storage performance of $Bi(Mg_{0.5}Ti_{0.5})O_3$ modified $Ba_{0.55}Sr_{0.45}TiO_3$ lead-free ceramics for pulsed power capacitors. *J. Eur. Ceram. Soc.* **2023**, *43*, 2426–2441. [CrossRef]
13. Choi, J.; Nkhama, A.; Kumar, A.; Mishra, S.R.; Perez, F.; Gupta, R.K. A facile preparation of sulfur doped nickel–iron nanostructures with improved her and supercapacitor performance. *Int. J. Hydrogen Energy* **2022**, *47*, 7511–7521. [CrossRef]

14. Nakate, U.T.; Patil, P.; Nakate, Y.T.; Na, S.I.; Hahn, Y.B. Ultrathin ternary metal oxide bi2moo6 nanosheets for high performance asymmetric supercapacitor and gas sensor applications. *Appl. Surf. Sci.* **2021**, *551*, 149422. [CrossRef]
15. Zhong, W.; Sun, H.; Pan, J.; Zhang, Y.; Cheng, X. Hierarchical porous tio2/carbide-derived carbon for asymmetric supercapacitor with enhanced electrochemical performance. *Mater. Sci. Semicond. Process.* **2021**, *127*, 105715. [CrossRef]
16. Cai, Y.; Kang, H.; Jiang, F.; Xu, L.; Xu, Q. The construction of hierarchical pedot@mos_2 nanocomposite for high-performance supercapacitor. *Appl. Surf. Sci.* **2021**, *546*, 149088. [CrossRef]
17. Song, Y.; Su, Z.; Zhao, Z.; Lin, S.; Wang, D. A new as3mo8v4/pani/rgo composite for high performance supercapacitor electrode–sciencedirect. *Ceram. Int.* **2021**, *47*, 21367–21372. [CrossRef]
18. Wang, G.; Yi, F.; Zhong, J.; Gao, A.; Liu, C.; Li, Q. Towards high-performance supercapacitor electrodes via achieving 3D cross-network and favorable surface chemistry. *ACS Appl. Mater. Interfaces* **2022**, *14*, 34637–34648. [CrossRef] [PubMed]
19. Yu, T.; Lei, X.; Chen, H.; Fan, K.; Wang, D.; Gao, Y. Conductive hydrogels with 2D/2D β-NiS/$Ti_3C_2T_x$ heterostructure for high-performance supercapacitor electrode materials. *Ceram. Int.* **2022**, *48*, 1382–1393. [CrossRef]
20. Tiwari, N.; Kadam, S.; Kulkarni, S. Synthesis and characterization of $ZnCO_2O_4$ electrode for high-performance supercapacitor application. *Mater. Lett.* **2021**, *298*, 130039. [CrossRef]
21. Liu, Y.; Zhang, J.; Wang, S.; Wang, K.; Chen, Z.; Xu, Q. Facilely constructing 3D porous $NiCo_2S_4$ nanonetworks for high-performance supercapacitors. *New J. Chem.* **2014**, *38*, 4045–4048. [CrossRef]
22. Lu, F.; Zhou, M.; Li, W.; Weng, Q.; Li, C.; Xue, Y.; Golberg, D. Engineering sulfur vacancies and impurities in $NiCo_2S_4$ nanostructures toward optimal supercapacitive performance. *Nano Energy* **2016**, *26*, 313–323. [CrossRef]
23. Zhang, X.; Wu, A.; Wang, X.; Tian, C.; An, R.; Fu, H. Porous NiCoP nanosheets as efficient and stable positive electrodes for advanced asymmetric supercapacitors. *J. Mater. Chem. A* **2018**, *6*, 17905–17914. [CrossRef]
24. Liu, T.; Zheng, Y.; Zhao, W.; Cui, L.; Liu, J. Uniform generation of $NiCo_2S_4$ with 3D honeycomb-like network structure on carbon cloth as advanced electrode materials for flexible supercapacitors. *J. Colloid Interface Sci.* **2019**, *556*, 743–752. [CrossRef] [PubMed]
25. Zhao, J.; Wang, Y.; Qian, Y.; Jin, H.; Tang, X.; Huang, Z.; Lou, L.; Zhang, Q.; Lei, Y.; Wang, S. Hierarchical design of cross-linked $NiCo_2S_4$ nanowires bridged NiCo-hydrocarbonate polyhedrons for high-performance asymmetric supercapacitor. *Adv. Funct. Mater.* **2023**, *33*, 2210238. [CrossRef]
26. Barik, R.; Ingole, P.P. Challenges and prospects of metal sulfide materials for supercapacitors. *Curr. Opin. Electrochem.* **2020**, *21*, 327–334. [CrossRef]
27. Mei, L.; Yang, T.; Xu, C.; Zhang, M.; Chen, L.; Li, Q.; Wang, T. Hierarchical mushroom-like $CoNi_2S_4$ arrays as a novel electrode material for supercapacitors. *Nano Energy* **2014**, *3*, 36–45. [CrossRef]
28. Guo, Y.; Wang, T.; Chen, X.; Wu, D. Agar-based porous electrode and electrolyte for flexible symmetric supercapacitors with ultrahigh energy density. *J. Power Sources* **2021**, *507*, 230252. [CrossRef]
29. Yu, X.; Wang, M.; Gagnoud, A.; Fautrelle, Y.; Ren, Z.; Li, X. Formation of highly porous $NiCo_2S_4$ discs with enhanced pseudocapacitive properties through sequential ion-exchange. *Mater. Des.* **2018**, *145*, 135–143. [CrossRef]
30. Xiang, G.; Meng, Y.; Qu, G.; Yin, J.; Teng, B.; Wei, Q.; Xu, X. Dual-functional $NiCo_2S_4$ polyhedral architecture with superior electrochemical performance for supercapacitors and lithium-ion batteries. *Sci. Bull.* **2020**, *65*, 443–451. [CrossRef]
31. Sahoo, M.K.; Rao, G. Fabrication of $NiCo_2S_4$ nanoball embedded nitrogen doped mesoporous carbon on nickel foam as an advanced charge storage material. *Electrochim. Acta* **2018**, *268*, 139–149. [CrossRef]
32. Xuan, H.; Guan, Y.; Han, X.; Liang, X.; Xie, Z.; Han, P.; Wu, Y. Hierarchical MnCo-LDH/rGO@ $NiCo_2S_4$ heterostructures on Ni foam with enhanced electrochemical properties for battery-supercapacitors. *Electrochim. Acta* **2020**, *335*, 135691. [CrossRef]
33. Long, Y.W.; Zeng, H.Y.; Li, H.B.; Zou, K.M.; Xu, S.; Cao, X.J. Sulfidation of CoAl-layered double hydroxide on Ni foam for high-performance supercapacitors. *Electrochim. Acta* **2020**, *361*, 137098. [CrossRef]
34. Cai, D.; Wang, D.; Wang, C.; Liu, B.; Wang, L.; Liu, Y.; Wang, T. Construction of desirable $NiCo_2S_4$ nanotube arrays on nickel foamsubstrate for pseudocapacitors with enhanced performance. *Electrochim. Acta* **2015**, *151*, 35–41. [CrossRef]
35. Jia, S.; Wei, J.; Gong, B.; Shao, Z. Sulfur vacancies enriched Nickel-Cobalt sulfides hollow spheres with high performance for All-Solid-State hybrid supercapacitor. *J. Colloid Interface Sci.* **2021**, *601*, 640–649. [CrossRef] [PubMed]
36. Anil Kumar, Y.; Yadav, A.A.; Al-Asbahi, B.A.; Kang, S.W.; Moniruzzaman, M. Sulfur Nanoparticle-Decorated Nickel Cobalt Sulfide Hetero-Nanostructures with Enhanced Energy Storage for High-Performance Supercapacitors. *Molecules* **2022**, *27*, 7458. [CrossRef]
37. Miao, P.; He, J.; Sang, Z.; Zhang, F.; Guo, J.; Su, D.; Ji, H. Hydrothermal growth of 3D graphene on nickel foam as a substrate of nickel-cobalt-sulfur for high-performance supercapacitors. *J. Alloys Compd.* **2018**, *732*, 613–623. [CrossRef]
38. Poompiew, N.; Pattananuwat, P.; Potiyaraj, P. In situ hydrothermal synthesis of nickel cobalt sulfide nanoparticles embedded on nitrogen and sulfur dual doped graphene for a high performance supercapacitor electrode. *RSC Adv.* **2021**, *11*, 25057–25067. [CrossRef]
39. Hu, Y.; Zhang, J.; Wang, D.; Sun, J.; Zhang, L.; Liu, Y.; Cui, Y. Urchin-like $NiCo_2S_4$ structures synthesized through a one-step solvothermal process for high-performance supercapacitors. *Particuology* **2019**, *45*, 66–73. [CrossRef]

40. Liu, B.L.; Ma, Y.X.; Wang, J.W.; Kang, X.Y.; He, L.J.; Lei, L.; Ran, F. Fabrication of nickel cobalt bimetallic sulfide doped graphite carbon nanohybrids as electrode materials for supercapacitors. *Diam. Relat. Mater.* **2022**, *124*, 108955. [CrossRef]
41. Dong, M.; Wang, Z.; Wang, J.; Guo, H.; Li, X.; Yan, G. Controlled Synthesis of $Ni_xCo_yS_4$/rGO Composites for Constructing High-Performance Asymmetric Supercapacitor. *Front. Mater.* **2019**, *6*, 176. [CrossRef]